Stability of ultrathin amorphous carbon films deposited on smooth silicon substrates by radio frequency sputtering

W. Lu and K. Komvopoulos
Department of Mechanical Engineering, University of California, Berkeley, California 94720
S. W. Yeh
Chevron Technology Research Center, Richmond, California 94700

Abstract

The mechanical stability of amorphous carbon (a-C) films deposited on ultrasmooth Si(100) substrates by radio-frequency sputtering under different energetic ion bombardment conditions was investigated in light of results obtained from aging and annealing experiments. The a-C films were annealed at 495 ^{o}C in the high-vacuum chamber of an x-ray photoelectron spectroscopy (XPS) system with a base pressure of 10^{-8} Torr. The annealing process consisted of three sequential heating cycles of temperature 495 ^{o}C and duration 5, 10, and 70 min, respectively. Atomic force microscopy and XPS studies were conducted to reveal possible changes in the surface topography, microstructure, and composition of the a-C films. To investigate the effect of annealing on the nanomechanical properties of the a-C films, nanoindentation experiments were performed with a surface force microscope. Only subtle changes in the surface topography, microstructure, composition, and nanomechanical properties of the a-C films were observed after aging for about two years. Film agglomeration during annealing due to residual stress relaxation was found to strongly depend on the kinetics of film deposition. It is shown that the stability of the a-C films is affected by residual stresses produced from the energetic ion bombardment during film growth. The magnitude of the residual stress and the film thickness exhibits a pronounced effect on the thermodynamics and kinetics of film agglomeration. The experimental results demonstrate that increasing the residual stress and/or film thickness decreases the mechanical stability of the a-C films.

Submitted to *Journal of Applied Physics* on July 11, 2000.

I. INTRODUCTION

Continuous and stable amorphous carbon (a-C) films with thickness only a few nanometers and superior nanomechanical and nanotribological properties are of great importance to several leading-edge technologies, such as microelectronic and information storage devices. Different film deposition techniques, both traditional and recently innovated, such as sputtering[1-3] and filtered cathodic arc deposition,[4] have been used to synthesize ultrathin, protective overcoats. In most of these film deposition techniques,[5] energetic species are used to synthesize dense, stable, and continuous ultrathin overcoats for wear and corrosion protection. However, results on the stability of plasma-deposited amorphous hydrogenated boron films[6] indicate that while intensive energetic ion bombardment improves the chemical stability by enhancing densification of the growing thin films, it may also degrade the film mechanical stability due to the high residual stresses produced during film growth.

The thermal stability of thin a-C films has been investigated by annealing the films in vacuum,[7-13] under controlled environments,[14,15] and even ambient air,[13] using different techniques to monitor changes in the microstructure and surface topography of the films. For instance, visible Raman spectroscopy was used to study the thermal stability and relaxation behavior of annealed a-C films with different sp^3 carbon contents.[8] Comparison of the changes in annealed a-C films with up to 85% sp^3 carbon contents, detected by surface-sensitive near edge x-ray absorption fine structure spectroscopy and two bulk-sensitive techniques, such as Raman spectroscopy and nanoindentation, demonstrated that hard a-C films synthesized by cathodic arc deposition exhibited high thermal stability up to about 800 ^{o}C.[9] Changes of the electrical conductivity and optical properties, such as refractive index, due to annealing were monitored in order to study the thermal stability of a-C films deposited by pulsed laser deposition.[16] Electrical conductivity measurements were used to study phase transitions from sp^3 to sp^2 carbon bonding

configurations and to correlate these phase changes to stress relaxation of annealed films.[12] This is because stress relaxation is believed to occur by a series of first order chemical reactions involving the conversion of sp^3 carbon atoms to sp^2 carbon atoms, and the exponential dependence of the electrical conductivity on the amount of converted sp^2 carbon atoms. The fraction of sp^2 carbon, surface roughness, internal stress, and hardness of nitrogenated carbon films deposited by radio frequency (rf) magnetron sputtering were all found to increase with increasing annealing temperature.[11] The loss of nitrogen and the structural modifications induced by thermal annealing were attributed to a change in the film microstructures from a soft paracyanogen-like material to a harder and more graphitic material.

High compressive residual stresses (4-14 GPa) in sputtered a-C films were associated with the kinetic energy of bombarding Ar ions during film growth,[17] while the substrate temperature was maintained below 70 ^{o}C. Since the compressive residual stresses in the films were believed to arise from ion peening, i.e., energetic ion bombardment, they were correlated to the ion kinetic energy. Compressive residual stresses in rf sputtered a-C films have been interpreted in terms of the power density, i.e., the product of the ion current density and bombarding kinetic energy.[2] Residual stresses (compressive or tensile) have been reported to be detrimental to the stability of thin films.[18] However, thick a-C films have been successfully fabricated by the sequential deposition of layers which were post-deposition annealed[19] or by the deposition of a stress-relaxation layer consisting of soft carbon.[20] However, basic understanding of the relaxation kinetics of unstable thin films, especially ultrathin a-C films, is rather limited.

In order to study the stability of rf sputtered ultrathin a-C films and to elucidate its dependence on the film deposition conditions, such as energetic ion bombardment, XPS, atomic force microscopy (AFM), and surface force microscopy (SFM) were used to monitor changes in the composition, microstructure, surface topography, and nanomechanical properties of the films

due to aging in ambient environments and high-vacuum annealing. To obtain insight into the effect of residual stress on the film relaxation process, the samples were exposed to three sequential annealing cycles in an XPS chamber. The dependence of the film mechanical properties on the film relaxation behavior was studied by performing indentations on the as-deposited, aged, and annealed a-C films. The thermodynamics and kinetics of film agglomeration are discussed in order to explain the effect of residual stresses on the stability of the ultrathin a-C films.

II. EXPERIMENTAL PROCEDURES

A. Film deposition and characterization

Ultrathin a-C films were deposited on smooth Si(100) substrates with a root-mean-square (rms) roughness of ~0.2 nm in pure Ar atmospheres using a modified rf sputtering system (Perkin-Elmer Randex, model 2400). Details about the film deposition procedures have been given elsewhere.[2] Films of thickness in the range of 10-70 nm, synthesized about two years ago under different energetic ion bombardment conditions, were selected for mechanical stability study. The deposition conditions (i.e., pressure p, rf power P, substrate bias voltage V_s, and deposition time t) of the examined a-C films are listed in Table I along with measured properties, such as root-mean-square (rms) surface roughness, thickness h, and nanoindentation hardness H. The corresponding film compositions are given in Table II. The film stability was studied by observing the changes in the surface morphology, microstructure, composition, and nanomechanical properties of the aged films before and after annealing in a high-vacuum environment. Changes in the surface topography were studied with an AFM (Nanoscope II, Digital Instruments). Surface imaging was performed in the contact mode with 10-nm-radius silicon tips. The typical size of the imaged surface topographies before annealing was 1 μm × 1 μm or 2 μm × 2 μm. Larger surface areas, up to 20 μm × 20 μm, of the annealed surfaces were

necessitated due to the significant roughening caused by film clustering and agglomeration. The nanomechanical properties of the a-C films were investigated with a SFM (Triboscope, Hysitron Inc.). A detailed description of this instrument, including the test and calibration procedures, has been given in previous publications.[1,21] Film nanohardness and elastic modulus measurements were obtained with a 20-nm-radius pyramidal diamond tip using an isosceles-triangle force profile with a maximum load of 20 μN and total loading/unloading time of 6 s. The SFM apparatus was used for both surface imaging and nanoindentation in order to facilitate the simultaneous study of the nanomechanical behavior of small surface features produced by annealing such as clusters.

B. High-vacuum annealing experiments

All the samples were simultaneously annealed in the high-vacuum chamber of a commercial XPS analysis equipment. Annealing involved heating the samples to a temperature of 495 ^{o}C for 5, 10, and 70 min following the sequence shown in Fig.1. The samples were fixed to a special copper block with screws to obtain high heat and electrical conduction such that the temperature of the sample surfaces to be reasonably close to that of the uniformly heated copper block. A thermocouple embedded to the back of the copper block was used to confirm that the temperature was maintained close to 495 ^{o}C during annealing. This temperature was selected in order to allow the in-situ study of microstructure changes caused by annealing. Before loading the samples, the copper block was heated to remove any adsorbed contaminants from its surface and also to estimate the heating and cooling rates in the high-vacuum chamber. Since heat transfer occurs predominantly by conduction through the sample holder in such a vacuum environment, cooling from 575 to 75 ^{o}C in a vacuum of about 10^{-8} Torr occurs in approximately 150 min. The vacuum pressure during annealing was about 3×10^{-7} Torr, and decreased rapidly to 10^{-8} Torr as soon as heating was terminated. XPS analyses were performed before annealing,

after each annealing cycle (when the sample temperature was less than 50 ^{o}C), and after the exposure of the annealed samples to the ambient environment in order to study the adsorption of airborne species on the annealed a-C film surfaces and their effects on the film microstructure.

C. XPS Analysis

Changes in the a-C film compositions due to each annealing cycle were monitored by XPS analysis conducted with a Kratos analytical XPS spectrometer with a monochromatic X-ray source of Al Kα (1486.6 eV). The XPS analysis was performed after the samples were cooled down to a merely ambient temperature. The spectrometer was operated at a constant pass energy of 20 eV. The analyzer resolution is equal to 2% of the pass energy. A 0.1 eV energy step was used to acquire the XPS spectra of the C 1s transitions. The approximately 2 mm × 0.5 mm spot illuminated by the Al Kα monochromator yielded an area resolution for the XPS analyzer of about 1 mm^2. To minimize uncertainties in the binding energy measurements, all the samples were mounted together on the same copper block for both annealing and XPS analysis. During the XPS analysis, the vacuum pressure was less than 5×10^{-9} Torr. The samples were not subjected to Ar ion bombardment for sputter cleaning before the XPS analysis.

The film compositions were determined from the intensities of characteristic core level peaks using published sensitivity factors. The a-C film microstructures were studied by deconvoluting the C 1s XPS peaks, after performing inelastic background subtraction using the method of Shirley,[22] and fitting with Gaussian distributions at characteristic binding energies following the method described by Sherwood.[23] The full-width half-magnitude (FWHM) values of the Gaussian profiles corresponding to the C 1s peaks were between 1.8 and 2.3 eV. Each Gaussian profile of the C 1s peaks was associated with a film constituent at a certain chemical state using characteristic binding energies at different environments.[24-27] The percentage of each constituent was determined from the calculated area under the corresponding Gaussian profile.

III. RESULTS AND DISCUSSION

A. Film composition and microstructure

Figure 2 shows representative XPS spectra of the aged film B obtained before and after annealing for different times. Qualitatively similar spectra were obtained for films A and C. Five different film constituents, i.e., C, O, N, Ar, and Si, were detected, as shown in Fig. 2(a). A significant decrease of the O peak occurred with increasing the time of annealing. A comparison of the as-deposited and aged film compositions, shown in Table II, reveals that aging produced very small changes in the film composition. A small increase in the N content and a decrease in the O content were detected in films A and C after the two-year exposure to the ambient conditions. In film B, besides the increase of the N content, both the O and the Si contents increased after aging. The presence of Si traces in the thinner film B may be attributed to surface contaminants and, presumably, diffusion of Si from the substrate.

Figure 3 shows the variation of the different constituents in the a-C films with annealing time. The origin of O, N, Ar, and Si in the a-C films has been discussed in a previous publication.[1] After annealing for 5 min, the carbon content increased by about 5 at% in all films, as shown in Fig. 3(a). While the carbon content of film A remained constant during further annealing, a gradual decrease by ~2.5 at% was observed for film B compared to a profound decrease by ~20 at% for film C. It will be shown later that this dramatic decrease in the carbon content of film C is because of the agglomeration of the film due to residual stress relaxation caused by the extensive annealing. The most likely sources of oxygen are vapors from the atmosphere physisorbed on the film surfaces upon exposure of the samples to the atmosphere and residual oxygen in the vacuum system incorporated in the films during deposition. The latter is confirmed by the annealing results. As shown in Fig. 3(b), in all three samples most of the oxygen was desorbed after annealing for 5 min, with only ~2 at% oxygen remaining in the a-C

films after annealing for a total of 85 min. The remaining oxygen is probably oxygen atoms incorporated in the films during growth, which were chemically bonded to carbon atoms. The small amount (~1 at%) of nitrogen in the a-C films [Fig. 3(c)] is attributed to the partial saturation of carbon dangling bonds on the fresh a-C film surfaces by the N_2 gas used to vent the chamber after film deposition,[1] and/or the incorporation of residual nitrogen from the chamber during film deposition. The chemically bonded nitrogen atoms remained in the films after annealing, while the physically adsorbed nitrogen atoms (~0.5 at%) were desorbed within 5 min of annealing.

The presence of silicon in films B and C [Fig. 3(d)] may be attributed to interdiffusion of silicon from the substrate or pinhole formation on the film surfaces due to stress relaxation. The latter is the most plausible explanation for the silicon detected in the a-C films, and is supported by surface topography results shown in Section III.B. The variations of the XPS intensities of the film and substrate materials were used to study the film coverage during film growth.[28] As suggested by the results shown in Fig. 3(d), the a-C films were almost continuous after annealing for 15 min. However, further annealing resulted in agglomeration of films B and C, which increased the silicon content by about 3 and 17 at%, respectively, due to the exposure of the substrate.

In addition to the carbon content, the structural composition of the carbon constituents in the a-C films was also changed due to annealing. Figure 4 shows deconvoluted C 1s XPS peaks of film C obtained at different stages of annealing. Four Gaussian profiles with characteristic binding energies were fitted to each C 1s peak after performing a Shirley inelastic background subtraction. The carbon peaks at binding energies of ~284.5 and ~285.6 eV (denoted by C 1s(1) and C 1s(2) in Table III) correspond to sp^2- and sp^3-coordinated carbon bonding in the a-C films.[1] The sp^2 and sp^3 carbon fractions in the amorphous phase can be estimated by using the

deconvolution method of the C 1s XPS spectra proposed by Jackson and Nuzzo[26] and Diaz et al.[27] The other two carbon peaks at binding energies of ~286.8 and ~288.4 eV (denoted by C 1s(3) and C 1s(4) in Table III) are respectively associated with sp^2 and sp^3 carbon atoms bonded to N, O, and other adsorbants on the film surface. The line positions and percentages of these features in the as-deposited and aged films (Table III) suggest that the effect of aging on the film microstructure was secondary. It can be seen from Table III that only ~20% of the carbon constituents in both the as-deposited and aged a-C films is pure sp^3 carbon and ~65% is pure sp^2 carbon. Therefore, the microstructures of the a-C films can be modeled as sp^3 carbon clusters dispersed in a matrix of sp^2 carbon with some of the sp^3 clusters bonded (chemically or physically) to contaminants, such as N and O, either incorporated in the films or adsorbed on the film surfaces.

Figures 5 and 6 show the variation of the binding energy and fraction of different carbon constituents in the a-C films with annealing time. The significant changes in the binding energies of the sp^2 and sp^3 carbon materials bonded with N and O contaminants observed after annealing for 5 min [Figs. 5(c) and 5(d)] are due to contaminant desorption from the film surfaces. To interpret the variation of the binding energies shown in Fig. 5, it is necessary to consider both the compositions of the a-C films and the carbon constituents in the films. The increase of the binding energies of C 1s(3) and C 1s(4) after annealing for 15 min is believed to be due to more complete desorption of the contaminants on the film surfaces. The further increase of the binding energy of C 1s(3) with time of annealing may be due to stress relaxation, while the decrease of the C 1s(4) binding energy is due to the loss of more N and O bonded to sp^3 carbon atoms. This is in agreement with the variations of the sp^2 and sp^3 percentages in the carbon constituents shown in Figs. 6(c) and 6(d), respectively.

From Figs. 6(a) and 6(b), it is evident that the percentages of pure sp^2 carbon decrease initially with annealing and then increase again, whereas the sp^3 carbon percentages exhibit an opposite trend. This can be interpreted in the context of the stress-induced phase transformation from sp^2 to sp^3 carbon in amorphous carbon materials.[17, 29-31] As suggested by Schwan et al.,[17] an extremely high compressive stress may cause pairs of sp^2 carbon sites to bond together to form sp^3 hybridized carbon. Due to thermal expansion coefficient differences between the highly densified a-C films and the substrate, and the low relaxation rate of the films at medium/high annealing temperatures, high compressive thermal stresses can be produced during the 5-min and 10-min annealing cycles. These compressive stresses may lead to a partial transformation of sp^2 carbon to sp^3 carbon during annealing, yielding an increase in the sp^3 fraction and a decrease in the sp^2 fraction, as shown in Figs. 6(a) and 6(b), respectively. Upon cooling down the samples after annealing for 15 min, strain misfits at boundaries of sp^3-carbon clusters and the sp^2-carbon matrix introduced a high stress in the sp^3 carbon phase. However, film relaxation through film agglomeration was not detected on any of the a-C films after annealing for 15 min, as evidenced from the XPS composition analysis shown in Fig. 3. This is the probable reason for the shift of the binding energy of C 1s(2) to lower values after annealing for 15 min, whereas the binding energy of C 1s(1) was affected only marginally, as shown in Figs. 5(b) and 5(a), respectively.

However, the 70-min annealing cycle promoted film relaxation. Thus, the high residual stress was relaxed and some sp^3 carbon configurations transformed into thermodynamically more stable sp^2 carbon configurations. The occurrence of film relaxation in the last annealing cycle was evidenced from (1) the decrease of the sp^3 carbon fraction and the increase of the sp^2 carbon fraction [Figs. 6(b) and 6(a), respectively], (2) the significant increase of the binding energy of C 1s(2) [Fig. 5(b)], and (3) the substrate exposure observed with films B and C [Fig. 3(d)].

B. Surface topography

AFM images of the surface topographies of the as-deposited and aged a-C films revealed insignificant changes in the surface roughness, indicative of the stability of the a-C films at ambient conditions. In view of the composition changes detected by XPS, it was expected that the surface topographies of the a-C films would differ after annealing. The increased surface reflectivity of annealed films B and C was thought to be due to a roughening effect. Figure 7 shows AFM images of the surface topographies of the a-C films before (left column) and after (right column) annealing. The rms surface roughness of annealed films A, B, and C (calculated from surface area images of 1 $\mu m \times 1$ μm, 5 $\mu m \times 5$ μm, and 20 $\mu m \times 20$ μm, respectively) was found equal to 0.92, 16.83, and 45.20 nm, respectively.

It is obvious from Figs. 7(a) and 7(b) that the surface topography of film A changed marginally after annealing. However, annealing of the relatively denser films B and C [Figs. 7(c) and 7(e)] resulted in significant pinhole formation [Fig. 7(d)] and agglomeration [Fig. 7(f)], even though they were subjected to identical annealing conditions. Despite the small change of the rms roughness of film A (from 0.90 to 0.92 nm) due to annealing, a comparison of Figs. 7(a) and 7(b) demonstrates the asperity coarsening occurred. Figure 8 shows the asperity height distribution (histogram) and bearing ratio curve (based on 100 divisions of the peak-to-valley distance) of film A before and after annealing. The zero value on the height axis in Fig. 8(a) represents the position of the mean planes of the surfaces. The depth in Fig. 8(b) was measured from the highest surface peak. It is obvious that annealing resulted in a broader asperity height distribution and a significant shift of the bearing area ratio, indicating a greater peak-to-valley distance after annealing.

Further annealing resulted in blistering and pinhole formation of the 10-nm-thick film B and profound agglomeration (clustering) of the 69-nm-thick film C. The nucleation and growth

of pinholes is considered to be the first stage of film agglomeration by surface diffusion of film constituents.[18] The holes on the exposed silicon substrate surface, shown in Fig. 7(f), are attributed to Ar atoms implanted in the substrate during the 3-min sputter-cleaning of the substrate surface by energetic Ar ion bombardment at ~850 eV. These holes are about 30-100 nm deep (measured with the AFM) and were formed during annealing due to the aggregation of Ar atoms in the silicon substrate. Similarly, in a study of the mechanical stability of diamondlike carbon films on silicon substrates with an aluminum interlayer subjected to vacuum heating,[32] the impairment of interfacial adhesion was argued to be a consequence of the release of Ar entrapped in the aluminum interlayer during sputter deposition, which promoted blister formation and film detachment. Therefore, the aggregation of implanted Ar atoms in the silicon substrate at the film/substrate interface is believed to play a critical role in film debonding (blistering) and pinhole nucleation.

As discussed earlier, the intensities of the Si 2p and C 1s peaks can be used to estimate the exposed substrate surface area. The tiny amount of silicon in the annealed film A detected by XPS suggests that the continuity of the film was not altered by the annealing process. Assuming that Si and C are not intermixed after annealing, the measured atomic percentages of Si and C in the annealed samples can be used to determine the area percentage of exposed substrate surface. Since the thickness of films B and C is significantly greater than the mean escape length of photoelectrons from the carbon film and silicon substrate, the atomic percentage of silicon and carbon measured by XPS can be approximated as

$$\frac{Si(at\%)}{C(at\%)} = \frac{\ddot{e}_{Si} \cdot x \cdot n_{Si} \cdot \acute{a}_{Si}}{\ddot{e}_{C} \cdot (1-x) \cdot n_{C} \cdot \acute{a}_{C}}, \quad (1)$$

where x represents the percentage of exposed substrate area, n is the atomic density of the materials, $\boldsymbol{l}_{\mathrm{Si}}$ and $\boldsymbol{l}_{\mathrm{C}}$ are the mean escape lengths of Si 2p photoelectrons in silicon and C 1s

photoelectrons in amorphous carbon, respectively (from methods in the literature,[33,34] it is found that $\lambda_{Si} \approx 4$ nm and $\lambda_C \approx 2$ nm), and α_{Si} and α_C are the photoelectron emissivities of Si and C atoms irradiated by the Al Kα X-ray (estimated to be 2×10^{-21} and 6×10^{-21} cm^2, respectively[35]). The density of films B and C was estimated[2] to be ~2.6 g/cm^3, while the density of single-crystal silicon is ~2.3 g/cm^3. Therefore, using the Si and C atomic percentages in the annealed films B and C, i.e., 3.24 at% Si and 92.57 at% C for film B and 17.31 at% Si and 77.69 at% C for film C, it is estimated that after the three annealing cycles the area percentage of exposed substrate surface is about 12% and 47% for films B and C, respectively. These values are in good agreement with the AFM images of the a-C films shown in Figs. 7(d) and 7(f).

The different film behaviors under identical annealing conditions (Fig.7) can be attributed to differences in the strain energy stored in the a-C films caused by changes in the intensity of energetic ion bombardment during film growth[2] and film thickness variations from 10 to 69 nm. It is well known that the residual stress and surface tension of the film and substrate materials and the film/substrate interface are critical to the film stability. Agglomeration of an initially continuous film occurs in three steps: hole nucleation, hole growth, and agglomeration to thermodynamically stable configurations.[18] Therefore, the effects of residual stress and film thickness on the response of the annealed films can be interpreted in terms of the thermodynamics and kinetics of agglomeration of stressed films deposited on a substrate.

The elastic strain energy per unit area in a continuous thin film under a uniform biaxial stress, bonded to a semi-infinite substrate, W^e, is given by

$$W^e = \frac{h \cdot (1-\nu_f) \cdot \sigma^2}{E_f} = h \cdot e, \quad (2)$$

where E_f and ν_f are the elastic modulus and Poisson's ratio of the film material, respectively, h is the film thickness, σ is the biaxial stress in the film, and e is the strain energy density. Stresses in

thin films can reach extremely high values, not possible in bulk materials, because of the small thickness and the reduced modes of plasticity and stress relaxation mechanisms, such as the nucleation and movement of dislocations. Thus, for continuous ultrathin films, changes in either the stress level or film thickness affect the strain energy stored in the film significantly, while the effect of the surface and interface energy of the film and substrate materials is negligible. Therefore, the stability of ultrathin films is very sensitive to changes in either the film thickness or stress level, i.e., the film stability degrades with increasing film thickness and/or internal stress.

For unstable or metastable thin films under stress, a new thermodynamic equilibrium must be reached by mechanisms that can increase the surface area and/or reduce the stress in the film. Surface roughening, film debonding, hole formation, and film agglomeration are examples of stress relaxation mechanisms. In view of the topography images shown in Fig. 7, it may be argued that the main mechanism leading to thermodynamic equilibrium in the a-C films of this study is agglomeration, although film debonding (blistering) also occurred in film B.

Residual (intrinsic) stresses in films also affect the kinetics of film agglomeration by changing the nucleation and growth rates of pinholes. This is because the coefficients of both lattice (bulk) and surface diffusion depend on the hydrostatic stress in the films. However, surface diffusion is expected to be dominant in the agglomeration process of ultrathin a-C films because of the significantly lower activation energy in surface diffusion compared to bulk diffusion. Therefore, stresses in ultrathin films not only reduce the film stability, but also accelerate the kinetics of film agglomeration. This is supported by the changes in the surface topography of the annealed a-C films. These findings demonstrate that the occurrence of different film agglomeration stages under identical annealing conditions is due to variations in the residual stress caused by differences in the energetic ion bombardment during film growth.

The effect of residual stress on the film stability was also demonstrated by sputtering a-C films on glass substrates using energetic ion bombardment during film growth. The deposition conditions were identical to those of film B. Figure 9 shows representative topographies characteristic of the pinhole and hillock formation stage [Fig. 9(a)] and the complete agglomeration stage [Fig. 9(b)]. This film is expected to have a high compressive residual stress due to the intensive energetic ion bombardment. The film was extremely smooth and continuous in the as-deposited condition. However, after exposure to the atmosphere, the film began to agglomerate at some surface areas and especially the edges where the stress concentration is higher. The image shown in Fig. 9(a), obtained at the boundary of continuous and agglomerated film areas, clearly shows the formation of pinholes and hillocks. Figure 9(b) shows a region where excessive film agglomeration occurred exposing the substrate surface.

C. Nanomechanical properties

Nanoindentation experiments performed before and after annealing with a 20-nm-radius pyramidal diamond tip under a maximum contact load of 20 μN revealed that, while aging degraded the nanomechanical properties only slightly, significantly lower hardness and elastic modulus values were obtained after annealing. The effect of aging and annealing on the nanohardness and in-plane elastic modulus of the a-C films is shown in Table IV. Nanoindentation of films B and C was cumbersome due to the film discontinuity, as shown in Fig. 7(f). Therefore, the measured hardness and elastic modulus of annealed film C are not very reliable. However, it was relatively easier to perform indentations on the surface of annealed film B because the pinhole-free surface areas were sufficient larger [Fig. 7(d)] than what is required for nanoindentation (about 100 nm $\times$ 100 nm). Thus, the measured nanohardness and elastic modulus of annealed film B are accurate and indicative of this film material.

Nanoindentation force versus displacement curves for films A and B obtained before and after annealing are shown in Figs. 10(a) and 10(b), respectively. The effect of annealing on the film nanomechanical behavior is apparent. The most pronounced changes pertain to the maximum contact depth and the slope of the unloading curves. The indentation curve of film A exhibits a greater hysteresis after annealing, indicative of the reduced resistance of plastic flow. The deformation of film B before annealing was essentially purely elastic; however, the force hysteresis obtained on the annealed film indicates that significant amount of work was dissipated in the softened film in the form of plastic deformation. The nanohardness and in-plane elastic modulus of the different films in the as-deposited, aged, and annealed conditions are compared in Figs. 11(a) and 11(b), respectively. It is evident that aging caused only a subtle reduction in the hardness and elastic modulus of all films, whereas annealing reduced both the hardness and the elastic modulus significantly, especially for films B and C. Energetic ion bombardment at 200 eV is the main reason for the higher hardness of films B and C in the as-deposited condition. The lower hardness of film C (compared to that of film B) is due to the longer exposure to ion bombardment that might have caused more damage and partial annealing of the film due to the increase of the surface temperature. However, the elastic modulus of film C is higher than that of film B. This may be due to the substrate effect, which becomes more pronounced as the film thickness decreases.[21] From the hardness values listed in Table IV, the decrease of the hardness of films A, B, and C due to aging is estimated to be about 13%, 12%, and 6%, respectively, whereas the corresponding decrease due to annealing is about 18%, 48%, and 60%. Similarly, the in-plane elastic modulus of films A, B, and C decreased due to aging by about 2%, 3%, and 11% and due to annealing by about 21%, 38%, and 70%, respectively.

In view of Fig. 7 and Table IV, it may be concluded that the effect of annealing on the surface topography and nanomechanical properties of the a-C films differed significantly. While

the surface topography characteristics of film A were marginally affected by annealing, the hardness and elastic modulus decreased appreciably. This softening effect of film A may be attributed to rearrangement of carbon atoms. However, the same annealing process not only reduced significantly the hardness and elastic modulus of film B, but also caused relaxation leading to blistering and pinhole formation. The effect of annealing on the integrity of film C was profoundly more severe. The film hardness and elastic modulus decreased dramatically, and excessive relaxation resulted in film agglomeration through long-range surface diffusion. The profoud differences in the relaxation process of the annealed films may be attributed to the remarkably different residual stresses due to energetic ion bombardment during film growth and differences in the film thickness.

Nanoindentation tests were also performed on the approximately circular blisters of film B, such as that shown in Fig. 12. By using the offsets of the AFM scanner to adjust the relative position of the tip, indentations were performed approximately at the center of the blisters. Figure 13 shows nanoindentation curves corresponding to a blister and a flat surface region where the film was still continuous and attached to the substrate. Nanoindentation of several blisters at different surface sites of the annealed film confirmed the repeatability of the representative indentation curve of the blister shown in Fig. 13. The remarkable change of the slopes of the loading and unloading portions of the indentation curve of the blister are indicative of the inward bending (loading) and partial recovery (unloading) of the indented blister. The greater slope (stiffening) observed after bending of the blister is due to contact of the blister dome with the underlying substrate.

D. Ar content and residual stress

Although the effect of the Ar content on the hardness and elastic modulus of rf sputtered a-C films has been reported to be negligibly small,[17] the Ar content provides information about

the plasma environment in which the films were grown[1] and the residual stress in the films.[1,2] Therefore, monitoring the changes of the Ar content and the binding energy of Ar 2p XPS transitions of the incorporated Ar atoms may yield some insight into the changes of the a-C films caused by annealing. The Ar 2p spectrum consists of two peaks: Ar $2p_{1/2}$ and Ar $2p_{3/2}$. The binding energy of each Ar 2p transition was determined as the position of a Gaussian distribution fitted to the particular peak. For all samples, the binding energy difference between Ar $2p_{1/2}$ and Ar $2p_{3/2}$ peaks is ~2.11 eV. Hence, hereafter the binding energy of Ar $2p_{3/2}$ electrons will be referred to as Ar 2p without any specification. Table V gives the Ar content and the binding energy of Ar 2p electrons of the as-deposited, aged, and annealed a-C films. The Ar content in the as-deposited films is in the range of 0.5-2.0 at%, depending on the deposition conditions. Although aging produced very small changes in the binding energy of Ar 2p electrons, it affected the Ar content in the films. The change of the Ar content may be also due to adsorbants on the film surfaces. Annealing reduced the Ar content in the films significantly, especially for the less dense film A (negligible energetic ion bombardment effect), and increased the binding energies of Ar 2p electrons. The increase of the binding energy of Ar 2p is related to stress relaxation of the a-C films due to annealing.[38] The annealed film B was selected for further study because of the higher Ar content and its relatively good surface condition. After exposure to the atmosphere, the O, N, and Si contents in film B increased from 2.49 at%, 1.00 at%, and 3.24 at% to 13.16 at%, 1.35 at%, and 3.37 at%, respectively, as determined from the XPS analysis. However, the binding energy of Ar 2p electrons and the Ar content changed only slightly from 241.82 ± 0.01 eV and 0.69 ± 0.01 at% to 241.80 ± 0.03 eV and 0.61 ± 0.08 at%, respectively. Therefore, investigating the changes of the binding energies of Ar 2p electrons due to annealing may provide insight into the residual stress in the film.

Although all the binding energies of Ar 2p listed in Table V are approximately 241.5 eV, i.e., close to that reported for Ar atoms embedded in graphite,[36] there are some important differences in the binding energies worthy of discussing. From Tables I and V, it can be observed that the binding energy of Ar 2p decreased with increasing energetic ion bombardment (see also Fig. 1 of Ref. 38). For zero substrate bias voltage, the binding energy of Ar 2p electrons is equal to 242.07 eV (film A), and decreased to 241.47 and 241.33 eV when the growing film was subjected to Ar ion bombardment at ~200 eV for 5 and 10 min, respectively (films B and C). Since Ar is an inert element, the binding energy shift of Ar 2p electrons can be associated with the mechanical environment established by the residual stress rather than the chemical environment in the a-C films.[38] During rf sputtering at low substrate temperatures, compressive stresses may occur in the films due to the effect of energetic ion bombardment. It has been reported[17,38] that carbon films deposited under conditions similar to those of films A-C possess residual biaxial compressive stresses in the range of 1-14 GPa.

Although the core levels of Ar atoms are not sensitive to strain, the work function (or chemical potential) is sensitive to the residual stress of the film. In the XPS analysis, the binding energy of core level electrons is obtained by measuring the kinetic energy of photoelectrons rather than measuring directly the energy gap between the core level and the vacuum level.[37] However, since the work function of the instrument is used to extract the binding energy information from the kinetic energy measurements (assuming that the samples are well grounded to the instrument), a shift of the measured binding energy of Ar 2p electrons is observed. The chemical potential change $\Delta\mu$ (assuming that the change of the atomic volume Ω is small and negligible) is given by

$$\Delta\mu = \pm\Delta\sigma \cdot \Omega, \tag{3}$$

where the positive and negative sign refer to tensile and compressive stress, respectively.[39] It was

found that the chemical potential change under a hydrostatic stress difference $\Delta\sigma$ = 6 GPa and the sensitivity $\Delta\mu/\Delta\sigma$ of the chemical potential change for an Ar atom are equal to 0.64 eV and 0.107 eV/GPa, respectively. From Table V, the difference between the measured binding energies of Ar 2p electrons of as-deposited films A and B is equal to 0.6 eV, which is very close to the calculated chemical potential change for a hydrostatic stress difference of 6 GPa. This method pf residual stress evaluation in thin films based on the binding energy shifts of Ar 2p electrons has been described in detail elsewhere.[38]

The blister dimensions can also be related to the residual stress in thin films. Based on a theoretical analysis of the debonding failure of a thin film under equi-biaxial compresion leading to the formation of a circular blister,[40,41] the equi-biaxial compressive stress σ in the unbuckled thin film can be expressed in terms of the radius R and the deflection δ at the center of a blister as

$$\frac{\delta}{h} \cong \left[\frac{1}{c_1}\left(\frac{\sigma}{\sigma_c} - 1\right)\right]^{1/2}, \tag{4}$$

and

$$\sigma_c = 1.2235 \frac{E_f}{1-\nu_f^{\,2}}\left(\frac{h}{R}\right)^2, \tag{5}$$

where σ_c is the critical stress at the instant of buckling and constant c_1 is given by $c_1 = 0.2473(1+\nu_f) + 0.2231(1-\nu_f^{\,2})$. These equations were derived by modeling the axisymmetrically buckled thin film as a completely clamped circular plate based on the von Karman nonlinear plate theory and assuming that R/t >> 1.[40] By combining Eqs. (4) and (5), the compressive stress σ in the film is given by

$$\sigma = \left[1 + c_1\left(\frac{\delta}{h}\right)^2\right] \cdot \left[1.2235 \frac{E_f}{1-\nu_f^{\,2}}\left(\frac{h}{R}\right)^2\right]. \tag{6}$$

Assuming the Poisson's ratio for the a-C films equal to 0.3, $c_1 \approx 0.5245$. The measured in-plane elastic modulus of the annealed film B is about 110.7 GPa (Table IV). Figure 14 shows blisters distributed over a 1-μm^2 surface area of the annealed film B. The dimensional parameters, such as δ and R, measured from ten different blisters of this surface image are listed in Table VI along with the calculated biaxial stress σ and hydrostatic stress σ_m. Based on the stress data given in Table IV, the hydrostatic (compressive) stress in the annealed film B is equal to 4.34 ± 1.24 GPa. Using the binding energies of Ar 2p electrons of annealed films A and B listed in Table V, the difference between the hydrostatic stresses of annealed films A and B calculated from Eq. (3) is equal to 4.95 GPa. Assuming that the residual stress in the annealed film A is close to zero (due to the nearly complete relaxation), the hydrostatic stress is estimated to be about -4.95 GPa, which is close to the above theoretical prediction using Eq. (6). It should be pointed out that the blister method yields estimates for the local stress because of the small imaged area and the blister dimensions, while the XPS method gives information about the residual stress over a relatively larger area, i.e., 1 μm^2 up to 1 mm^2 surface areas in this study.

IV. CONCLUSIONS

The stability of ultrathin a-C films sputtered on silicon substrates was investigated in light of changes in the film composition, microstructure, surface topography, and nanomechanical behavior caused by aging and annealing. Based on the presented results and discussion, the following main conclusions can be drawn.

1. Composition analysis of the annealed a-C films demonstrated that most of the oxygen and nitrogen was physisorbed on the film surfaces and only a small fraction was incorporated in the films during film growth.

2. The residual stress in the films due to the energetic ion bombardment during film deposition and the film thickness play important roles in the thermodynamics and kinetics of the film stability. The residual elastic strain energy degrades the film stability by changing the thermodynamic equilibrium of the film-substrate system and by accelerating the kinetics of film relaxation.
3. Amorphous carbon materials in the a-C films comprise mixtures of sp^3 carbon clusters dispersed in a matrix of sp^2 carbon material. The increase of the sp^3 carbon in the amorphous carbon material after annealing at 495 ^{o}C for 15 min is associated with a stress-induced phase transformation from sp^2 to sp^3 carbon hybridization.
4. Although aging produced only subtle changes to the mechanical properties of the a-C films, film relaxation due to annealing degraded the film properties significantly. The dominant mechanisms of film relaxation were blistering and agglomeration.
5. Small amounts of Ar atoms incorporated in the a-C films during film growth were used to estimate the residual stress based on the binding energy shifts of Ar 2p XPS transitions.
6. Film failure by blistering and agglomeration was observed after annealing the films deposited under a bias voltage (energetic ion bombardment effect). Based on the average dimensions of the blisters and a theoretical model from the literature, the hydrostatic compressive residual stress in partially relaxed annealed films was estimated to be about –4.3 GPa. While the residual stress is not uniform, the average value of the estimated residual stresses is in fair agreement with that obtained from the XPS method using a larger film surface area.

ACKNOWLEDGEMENT

This research was supported by the Surface Engineering and Tribology Program of the National Science Foundation under Grant No. CMS-9734907 and CML at UC-Berkeley.

REFERENCES

[1]W. Lu and K. Komvopoulos, J. Appl. Phys. **85**, 2642 (1999).

[2]W. Lu and K. Komvopoulos, J. Appl. Phys. **86**, 2268 (1999).

[3]W.C. Chan, B. Zhou, Y.W. Chung, C.S. Lee, and S.T. Lee, J. Vac. Sci. Technol. A **16**, 1907 (1998).

[4]C.S. Bhatia, S. Anders, I.G. Brown, K. Bobb, R. Hsiao, and D.B. Bogy, J. Tribol. **120**, 795 (1998).

[5]Y. Lifshitz, Diam. Relat. Mater. **5**, 388 (1996).

[6]A. Annen, M. Sass, R. Beckmann, and W. Jacob, Thin Solid Films **300**, 101 (1997).

[7]A.A. Ogwu, R.W. Lamberton, P.D. Maguire, and J.A. McLaughlin, J. Phys. D **32**, 981 (1999).

[8]R. Kalish, Y. Lifshitz, K. Nugent, and S. Prawer, Appl. Phys. Lett. **74**, 2936 (1999).

[9]S. Anders, J. Diaz, J.W. Ager III, R.Y. Lo, and D.B. Bogy, Appl. Phys. Lett. **71**, 3367 (1997).

[10]T.A. Friedmann, K.F. McCarty, J.C. Barbour, M.P. Siegal, and D.C. Dibble, Appl. Phys. Lett. **68**, 1643 (1996).

[11]M.M. Lacerda, F.L. Freire, R. Prioli, C.M. Lepinski, and G. Mariotto, J. Vac. Sci. Technol. A **17**, 2811 (1999).

[12]J.P. Sullivan, T.A. Friedmann, and A.G. Baca, J. Electr. Mater. **26**, 1021 (1997).

[13]S. Bhargavaa, H.D. Bist, A.V. Narlikar, S.B. Samanta, J. Narayan, and H.B. Tripathi, J. Appl. Phys. **79**, 1917 (1996).

[14]Q. Zhang, S.F. Yoon, Rusli, H. Yang, and J. Ahn, J. Appl. Phys. **83**, 1349 (1998).

[15]A. Callegari, D.A. Buchanan, H. Hovel, E. Simonyi, A. Marwick, and N.E. Lustig, Appl. Phys. Lett. **65**, 3200 (1994).

[16]C.W. Ong, X.A. Zhao, J.T. Cheung, S.K. Lam, Y. Liu, C.L. Choy, and P.W. Chan, Thin Solid Films **258**, 34 (1995).

[17]J. Schwan, S. Ulrich, H. Roth, H. Ehrhardt, S.R.P. Silva, J. Robertson, R. Samlenski, and R. Brenn, J. Appl. Phys. **79**, 1416 (1996).

[18]D.J. Srolovitz and M.G. Goldiner, JOM (TMS) **47**, 31 (1995).

[19]T.A. Friedmann, J.P. Sullivan, J.A. Knapp, D.R. Tallant, D.M. Follstaedt, D.L. Medlin, and P.B. Mirkarimi, Appl. Phys. Lett. **71**, 3820 (1997).

[20]M. Gioti, S. Logothetidis, and C. Charitidis, Appl. Phys. Lett. **73**, 184 (1998).

[21]W. Lu and K. Komvopoulos, J. Tribology, submitted (2000).

[22]D.A. Shirley, Phys. Rev. B **5**, 4709 (1972).

[23]P. Sherwood, in *Practical Surface Analysis by Auger and X-ray Photoelectron Spectroscopy*, edited by D. Briggs and M.P. Seah, John Wiley, New York, p.181 (1983).

[24]H. Sjostrom, L. Hultman, J.-E. Sundgren, S. V. Hainsworth, T. F. Page, and G. S. A. M. Theunussen, J. Vac. Sci. and Technol. A **14**, 56 (1996).

[25]S. Souto, M. Pickholz, M. C. dos Santos, and F. Alvarez, Phys. Rev. B **57**, 2536 (1998).

[26]S. T. Jackson, R. G. Nuzzo, Appl. Surf. Sci. **90**, 195 (1995).

[27]J. Diaz, G. Paolicelli, S. Ferrer, and F. Comin, Phys. Rev. B **54**, 8064 (1996).

[28]J.M. Slaughter, W. Weber, G. Guntherodt, and C. Falco, MRS Bulletin **17**, 39 (1992).

[29]D.R. McKenzie, D. Muller, and B.A. Pailthorpe, Phys. Rev. Lett. **67**, 773 (1991).

[30]S. Scandolo, M. Bernasconi, G.L. Chiarotti, P. Focher, and P. Tosatti, Phys. Rev. Lett. **74**, 4015 (1995).

[31]M. Kitabatake, Diamond Films Technol. **5**, 41 (1995).

[32]X.L. Peng and T.W. Clyne, Thin Solid Films **312**, 219 (1998).

[33]M.P. Seah and W.A. Dench, Surf. Interface Anal. **1**, 2 (1979).

[34]M.P. Seah, in *Practical Surface Analysis by Auger and X-ray Photoelectron Spectroscopy*, edited by D. Briggs and M.P. Seah, Wiley, New York, p.181 (1983).

[35]C.D. Wagner, in *Handbook of X-ray and Ultraviolet Photoelectron Spectroscopy*, edited by D. Briggs, Heyden, London, p. 249 (1977).

[36]K. S. Kim and N. Winograd, Chem. Phys. Lett. **30**, 91 (1975).

[37]S. Evans, in *Handbook of X-ray and Ultraviolet Photoelectron Spectroscopy*, edited by D. Briggs, Heyden, London, p. 121 (1977).

[38]W. Lu and K. Komvopoulos, Appl. Phys. Lett. **76**, 3206 (2000).

[39]K. N. Tu, J. W. Mayer, and L. C. Feldman, *Electronic Thin Film Science: For Electrical Engineers and Materials Scientists*, Macmillan, New York, 1992.

[40]J.W. Hutchinson and Z. Suo, in *Advances in Applied Mechanics*, Vol. **29**, edited by J.W. Hutchinson and T.Y. Wu, pp. 64, Academic Press, New York (1991).

[41]J.W. Hutchinson, M.D. Thouless, and E.G. Liniger, Acta Metall. Mater. **40**, 295 (1992).

Table I. Deposition conditions, surface roughness, film thickness, and nanoindentation hardness of as-deposited a-C films.

Film	Deposition conditions				Film properties		
	p (mTorr)	P (W)	V_s (V)	t (min)	rms (nm)	h (nm)	H (GPa)
A	3	750	0	5	0.90	27	19.67 ±1.41
B	3	750	-200	5	0.20	10	39.19 ±3.53
C	3	750	-200	10	0.15	69	31.83 ±1.82

Table II. Compositions of a-C films obtained from XPS analysis.

Film	Elemental composition (at%)									
	As-deposited					Aged				
	C	O	N	Si	Ar	C	O	N	Si	Ar
A	88.04	10.69	0.75	0.01	0.55	88.77	9.19	1.43	0.03	0.59
B	89.68	7.39	0.95	0.05	1.93	87.89	8.40	1.49	0.87	1.37
C	90.14	7.44	0.88	0.01	1.54	90.41	7.02	1.22	0.00	1.36

Table III. Binding energies (BE) of characteristic Gaussian profiles and corresponding atomic percentages in XPS spectra of rf sputtered a-C films.

Film	Line position and fraction	Constituents in amorphous carbon material							
		As-deposited				Aged			
		C 1s(1)	C 1s(2)	C 1s(3)	C 1s(4)	C 1s(1)	C 1s(2)	C 1s(3)	C 1s(4)
A	BE (eV)	284.45	285.44	286.72	288.35	284.55	285.68	286.90	288.55
	at%	66.61	18.16	8.16	5.37	68.53	15.23	8.98	3.64
B	BE (eV)	284.36	285.36	286.73	288.40	284.38	285.47	286.91	288.48
	at%	61.36	23.91	7.75	5.01	65.02	20.00	8.19	3.66
C	BE (eV)	284.24	285.38	286.65	287.90	284.38	285.54	286.88	288.44
	at%	64.76	18.82	5.23	6.14	64.10	17.94	9.16	3.30

Table IV. Nanoindentation hardness and in-plane elastic modulus of as-deposited, aged, and annealed a-C films.

Film	As-deposited		Aged		Annealed	
	H (GPa)	$E/(1-\nu^2)$ (GPa)	*H* (GPa)	$E/(1-\nu^2)$ (GPa)	*H* (GPa)	$E/(1-\nu^2)$ (GPa)
A	19.7 ±1.4	132.6 ±4.6	17.1 ±1.6	129.6 ±9.8	14.0 ±1.3	101.9 ±9.7
B	39.2 ±3.5	185.1 ±9.0	34.3 ±1.5	178.8 ±6.5	17.9 ±2.8	110.7 ±12.6
C	31.8 ±1.8	207.5 ±12.4	29.9 ±1.8	185.5 ±9.7	12.2 ±0.1	54.8 ±13.0

Table V. Ar content and binding energy of transition Ar $2p_{3/2}$ electrons of as-deposited, aged, and annealed a-C films.

Film	A		B		C	
Content and Binding energy	Ar (at%)	Ar $2p_{3/2}$ (eV)	Ar (at%)	Ar $2p_{3/2}$ (eV)	Ar (at%)	Ar $2p_{3/2}$ (eV)
As-deposited	0.55	242.07	1.93	241.47	1.54	241.33
Aged	0.59	242.07	1.37	241.49	1.36	241.44
Annealed (5min)	0.23	242.21	1.17	241.55	1.04	241.50
Annealed (15min)	0.13	242.24	1.12	241.57	1.02	241.51
Annealed (85min)	0.04	242.35	0.69	241.82	0.80	242.15

Table VI. Calculated residual biaxial and hydrostatic stresses in the annealed film B.

Blister	δ (nm)	*R* (nm)	σ (GPa)	σ_m (GPa)
1	17.8	87	-4.76	-3.18
2	18	90	-4.51	-3.01
3	16	80	-4.96	-3.31
4	19	85	-5.42	-3.62
5	48	132	-10.17	-6.78
6	36.5	110	-8.94	-5.96
7	10.2	60	-5.82	-3.88
8	11.8	60	-6.51	-4.34
9	12	60	-6.60	-4.40
10	20	75	-7.46	-4.97

List of figures

FIG. 1. Sequential annealing cycles of (a) 5 min, (b) 10 min, and (c) 70 min heating at 495 ^{o}C in a high vacuum.

FIG. 2. XPS spectra of film B obtained before annealing (a) and after annealing for (b) 5 min, (c) 15 min, and (d) 85 min.

FIG. 3. Variation of constituents of films A-C with annealing time: (a) C, (b) O, (c) N, and (d) Si.

FIG. 4. C 1s XPS spectra with Gaussian fits of film B obtained before annealing (a) and after annealing for (b) 5 min, (c) 15 min, and (d) 85 min.

FIG. 5. Binding energies of characteristic Gaussian fits of C 1s versus annealing time.

FIG. 6. Fractions of characteristic Gaussian fits of C 1s versus annealing time.

FIG. 7. AFM images of film surface topographies obtained before annealing (first column) and after annealing (second column): (a) and (b) film A; (c) and (d) film B; (e) and (f) film C.

FIG. 8. (a) Histogram and (b) bearing ratio curves for film A obtained before and after annealing corresponding to the AFM images shown in Figs. 7(a) and 7(b).

FIG. 9. AFM images of surface topographies of (a) partially and (b) completely agglomerated a-C films on a glass substrate. (The deposition conditions are identical to those of film B.)

FIG. 10. Comparison of nanoindentation curves of (a) film A and (b) film B obtained before and after annealing.

FIG. 11. Effect of aging and annealing on (a) film nanohardness and (b) in-plane elastic modulus of different a-C films.

FIG. 12. AFM image of a blister on the surface of annealed film B indented by a 20-nm-radius diamond tip.

FIG. 13. Nanoindentation curves obtained from a continuous surface region and a blister of annealed film B.

FIG. 14. AFM images of blisters on the surface of annealed film B obtained with a the 20-nm-radius diamond tip under a contact force of 1 μN.

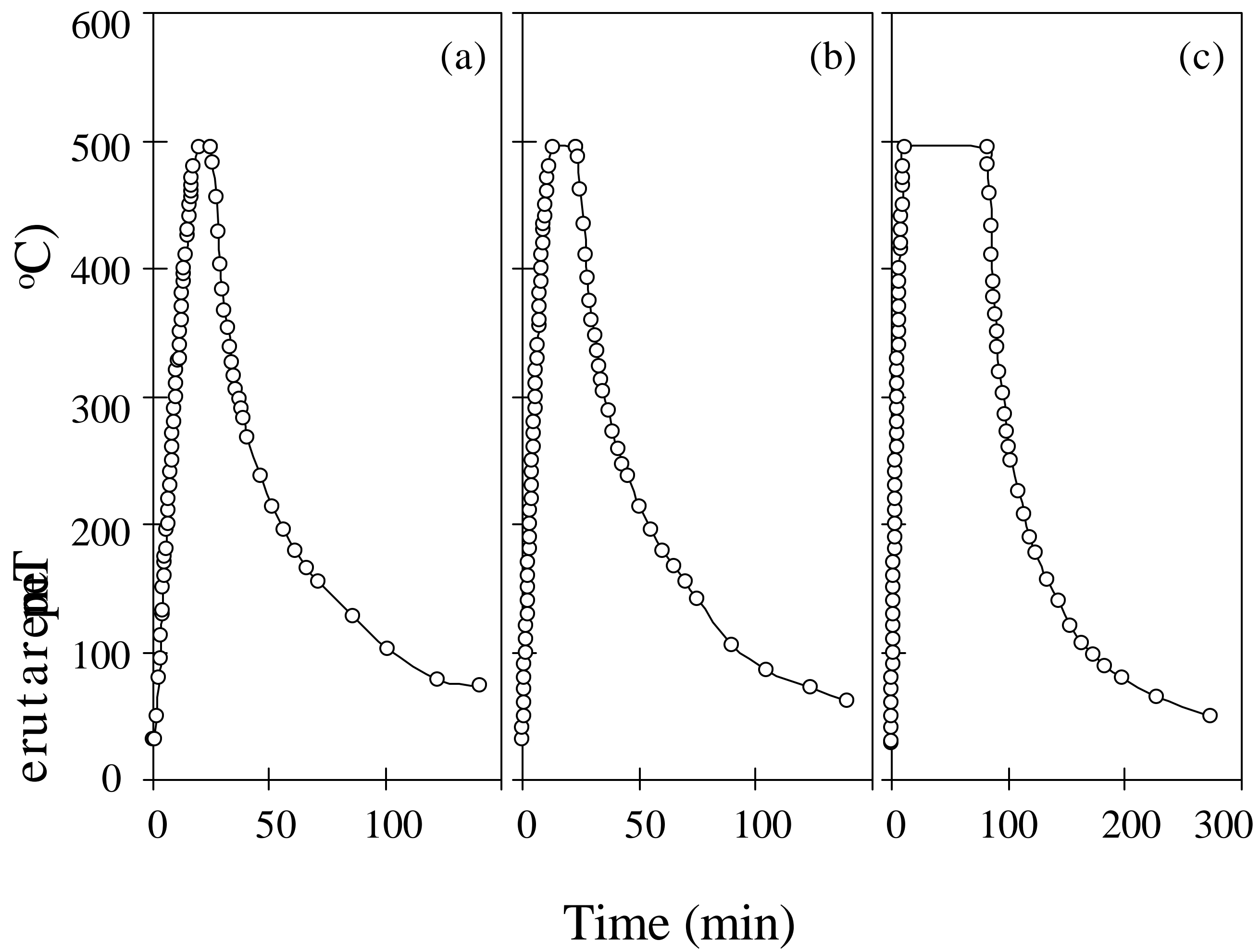

Figure 1

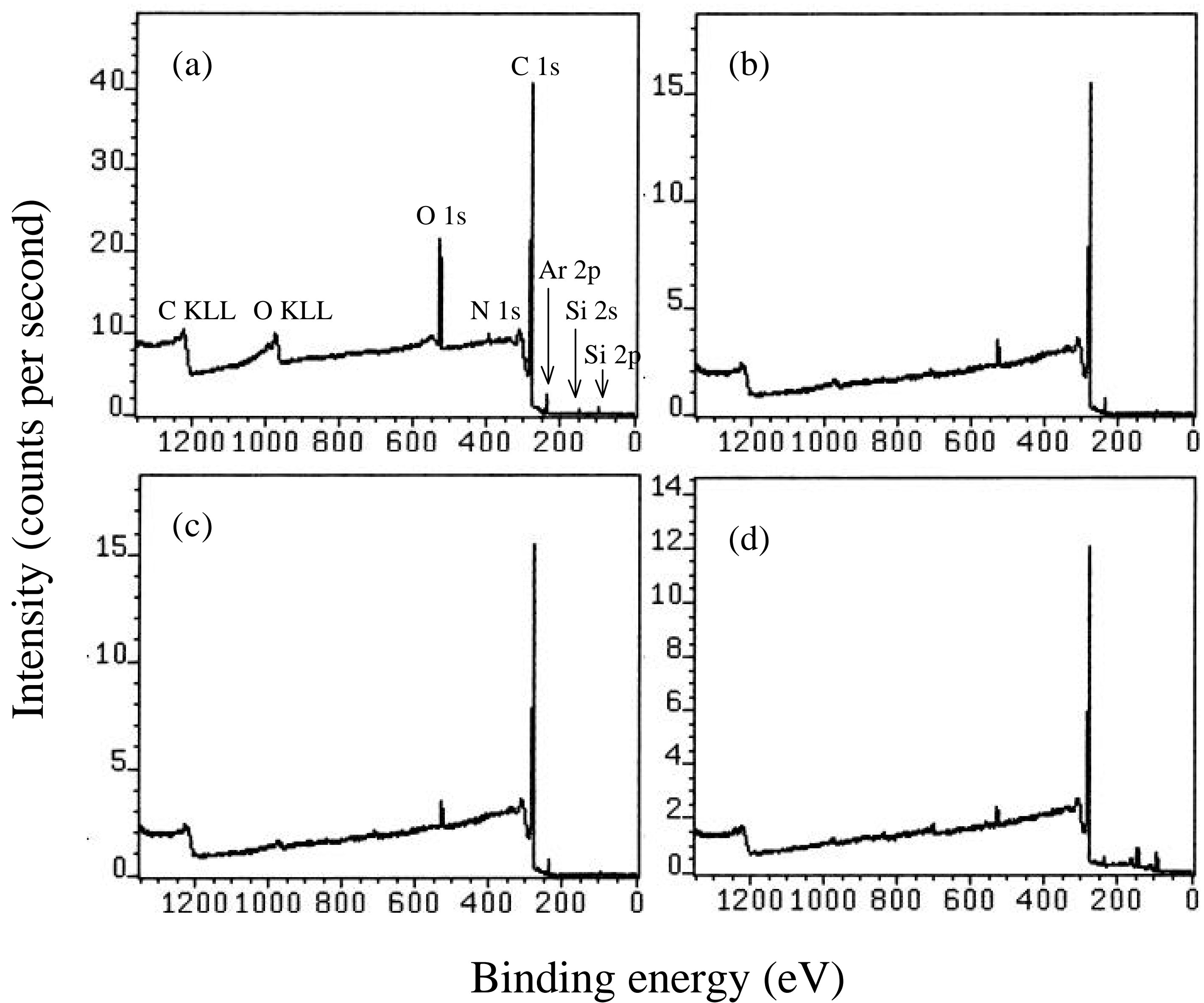

Figure 2

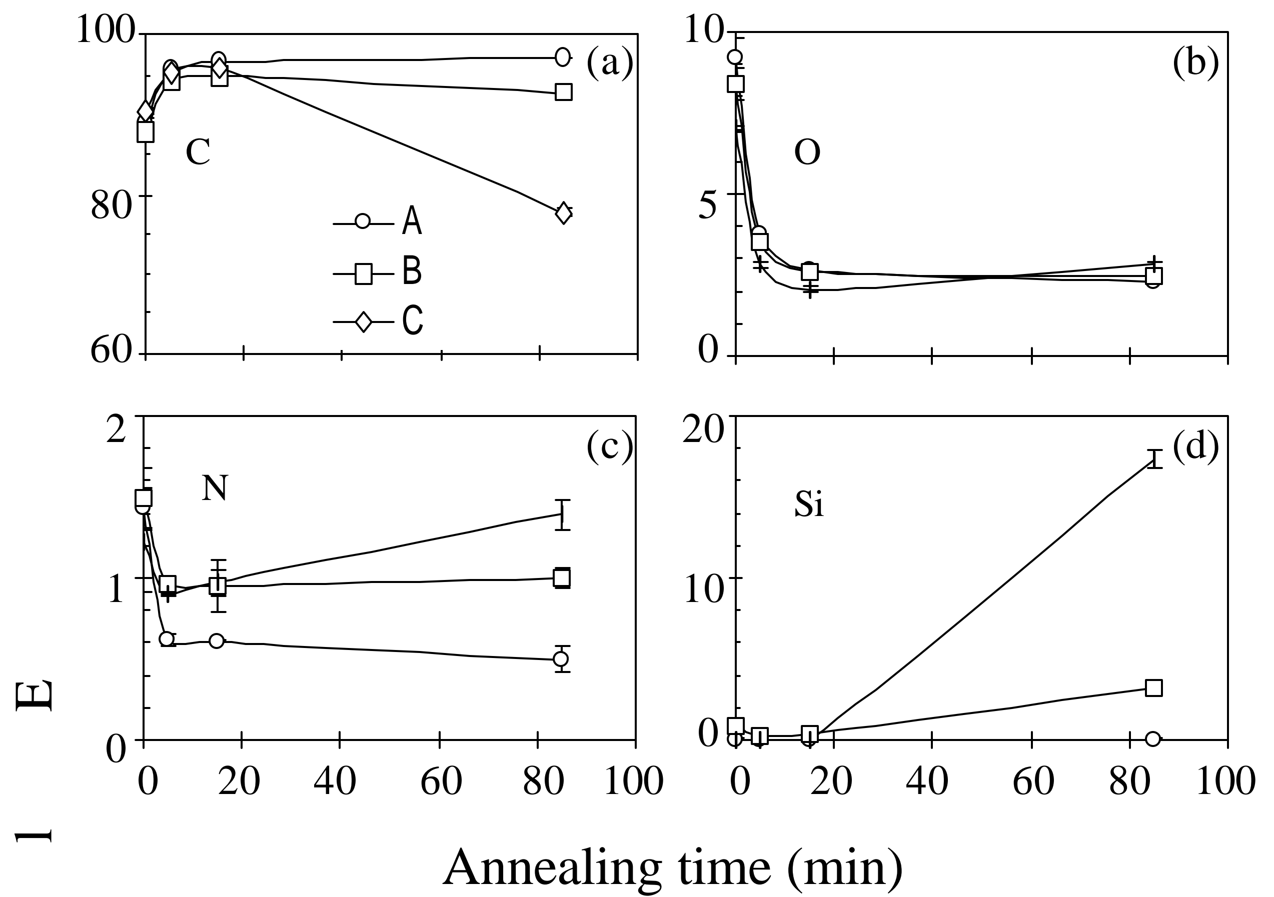

Figure 3

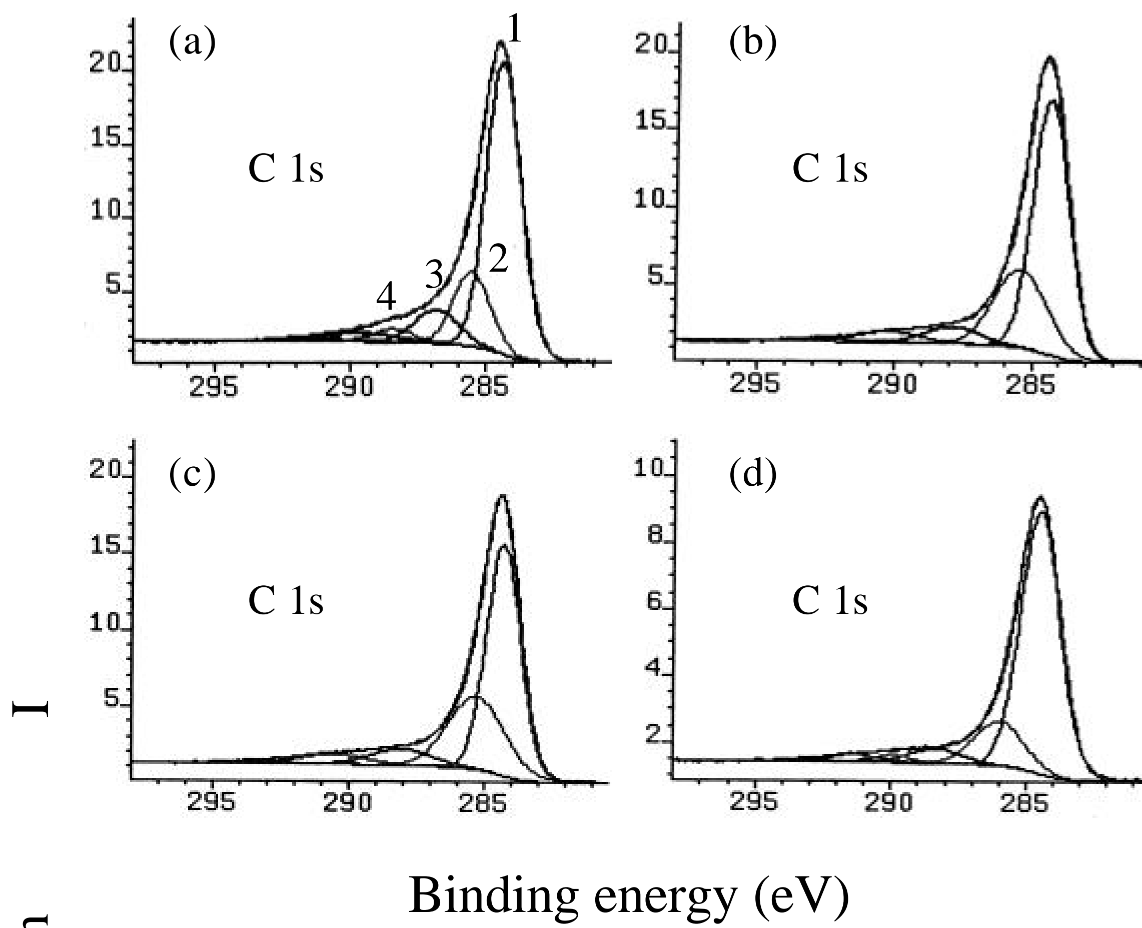

Figure 4

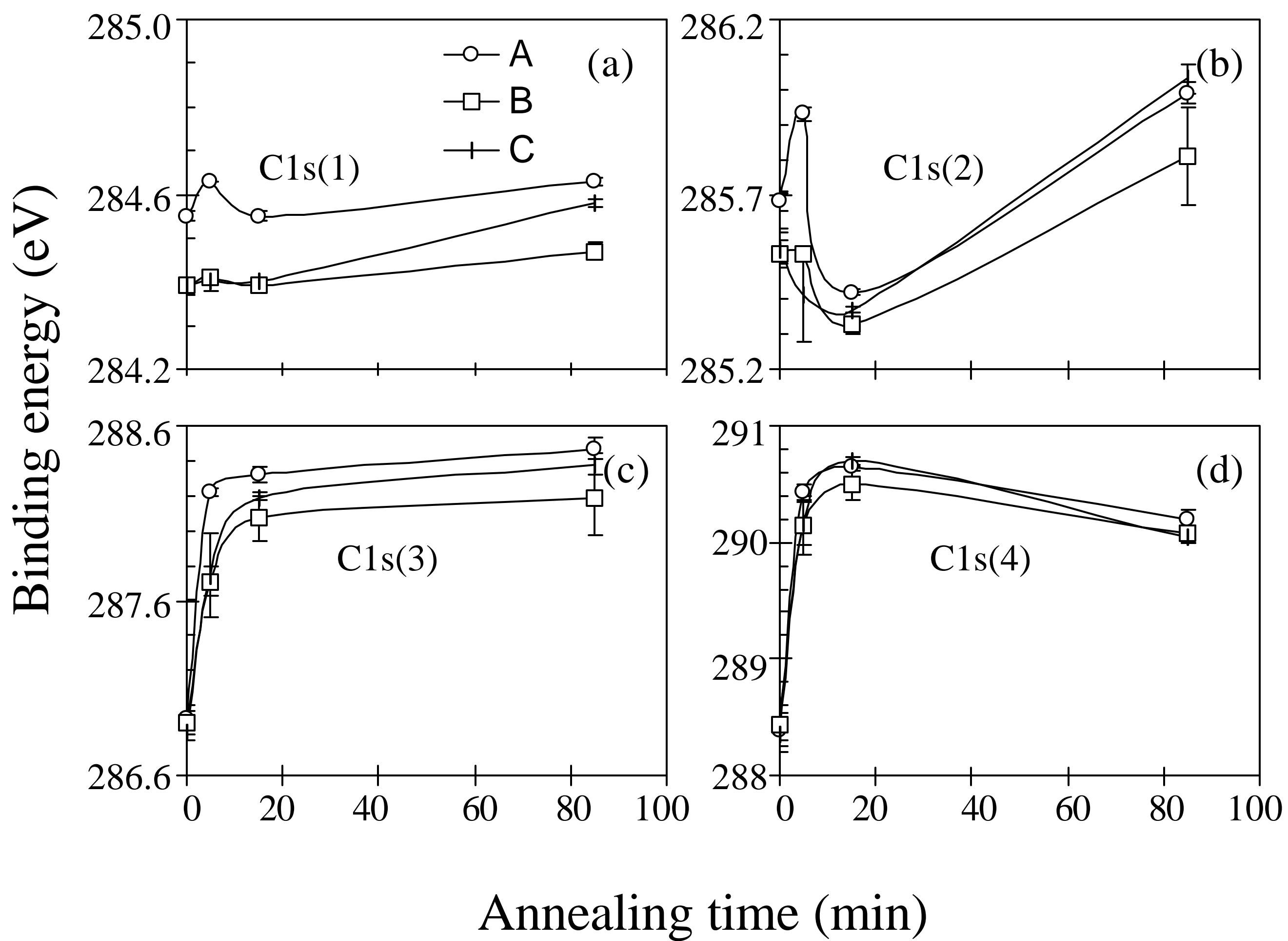

Figure 5

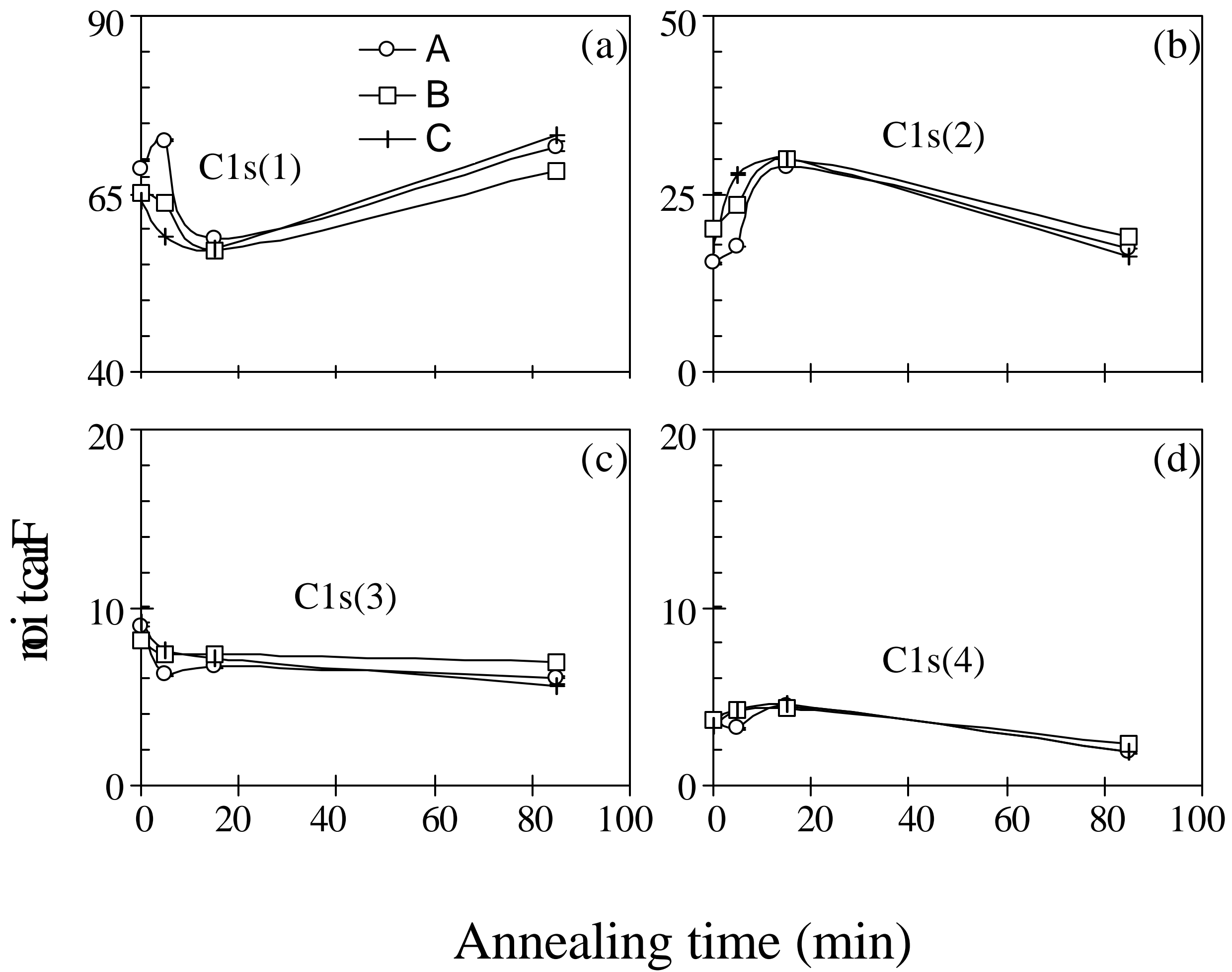

Figure 6

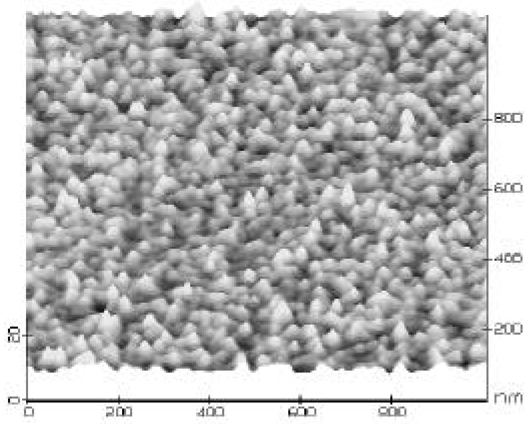

(a)

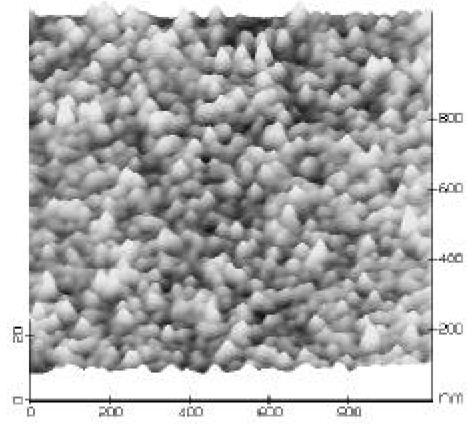

(b)

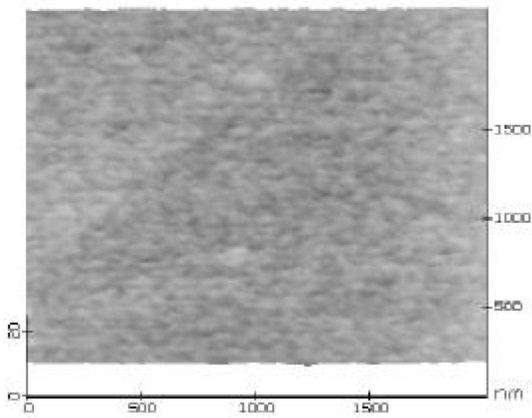

(c)

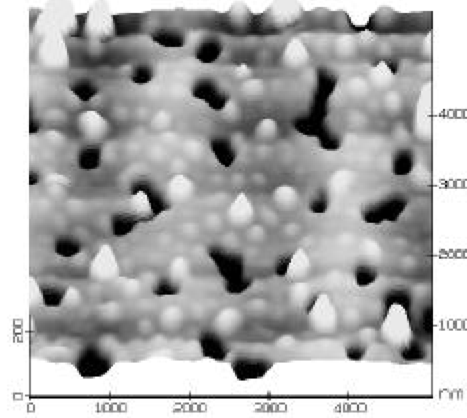

(d)

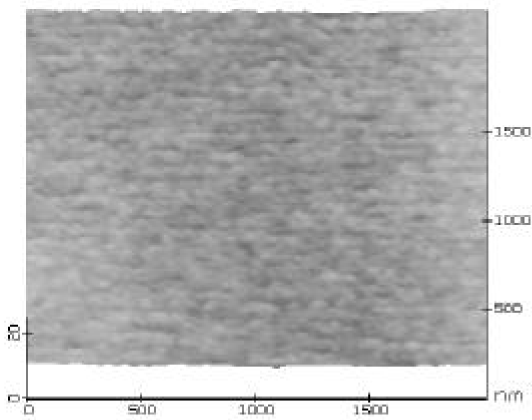

(e)

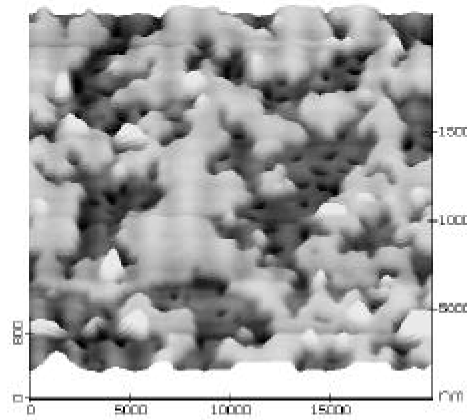

(f)

Figure 7

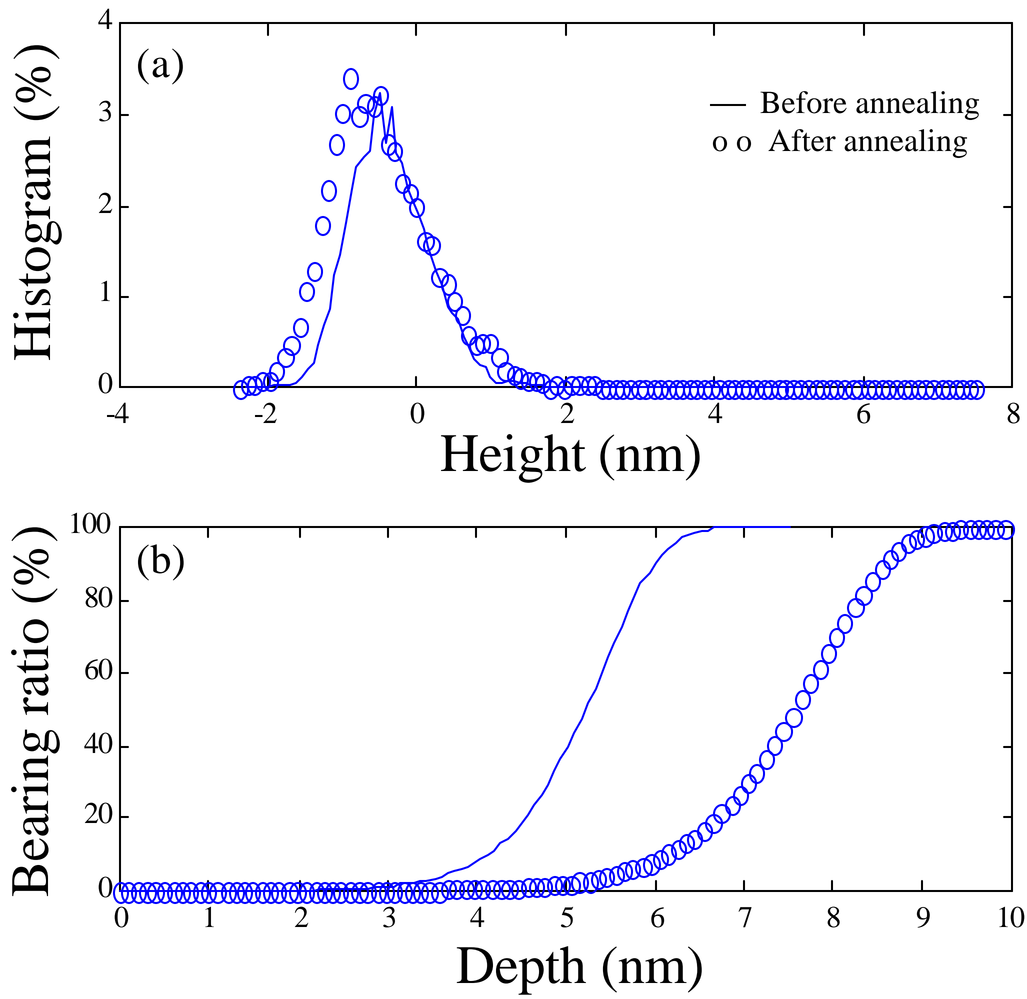

Figure 8

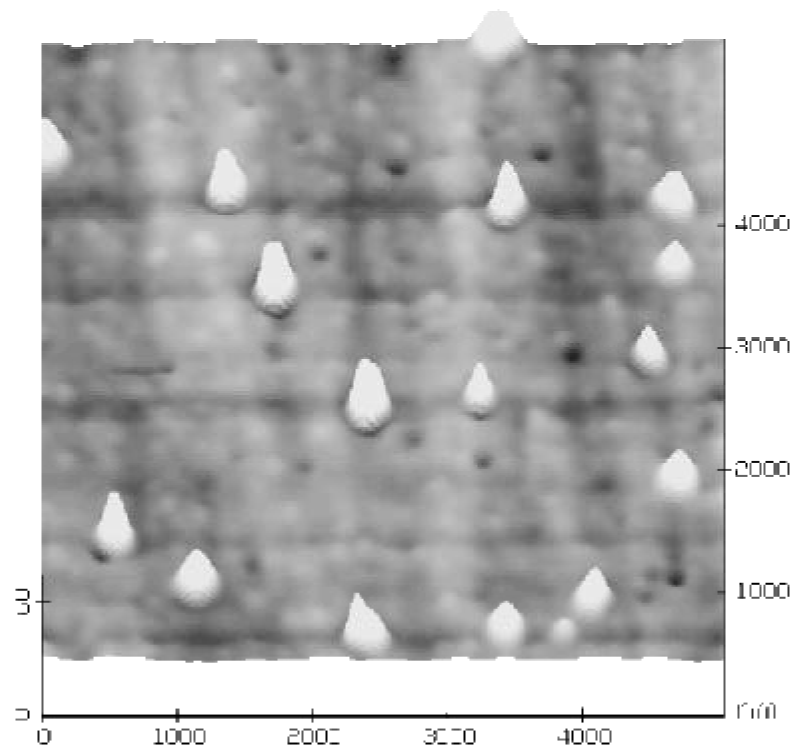

(a)

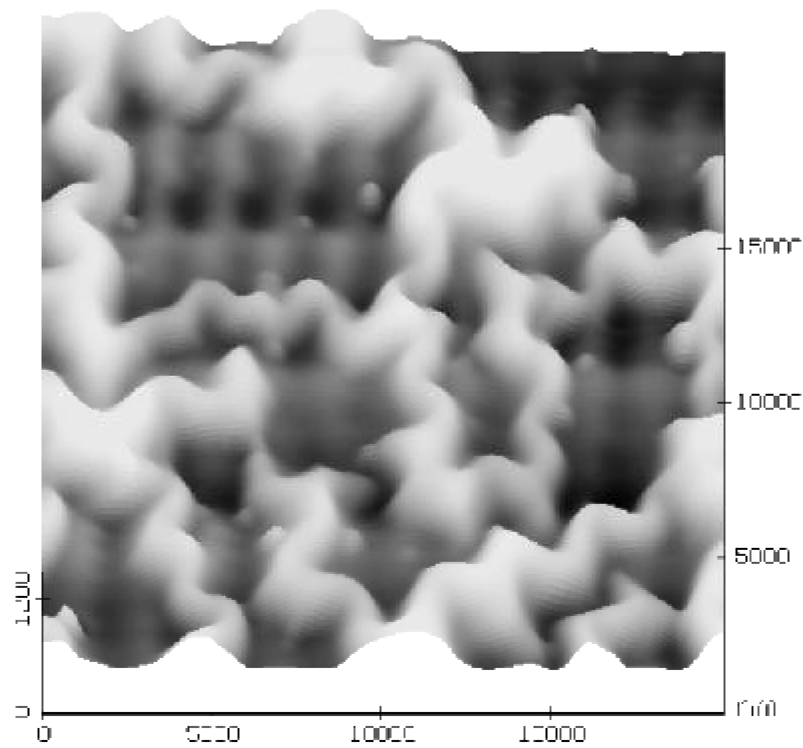

(b)

Figure 9

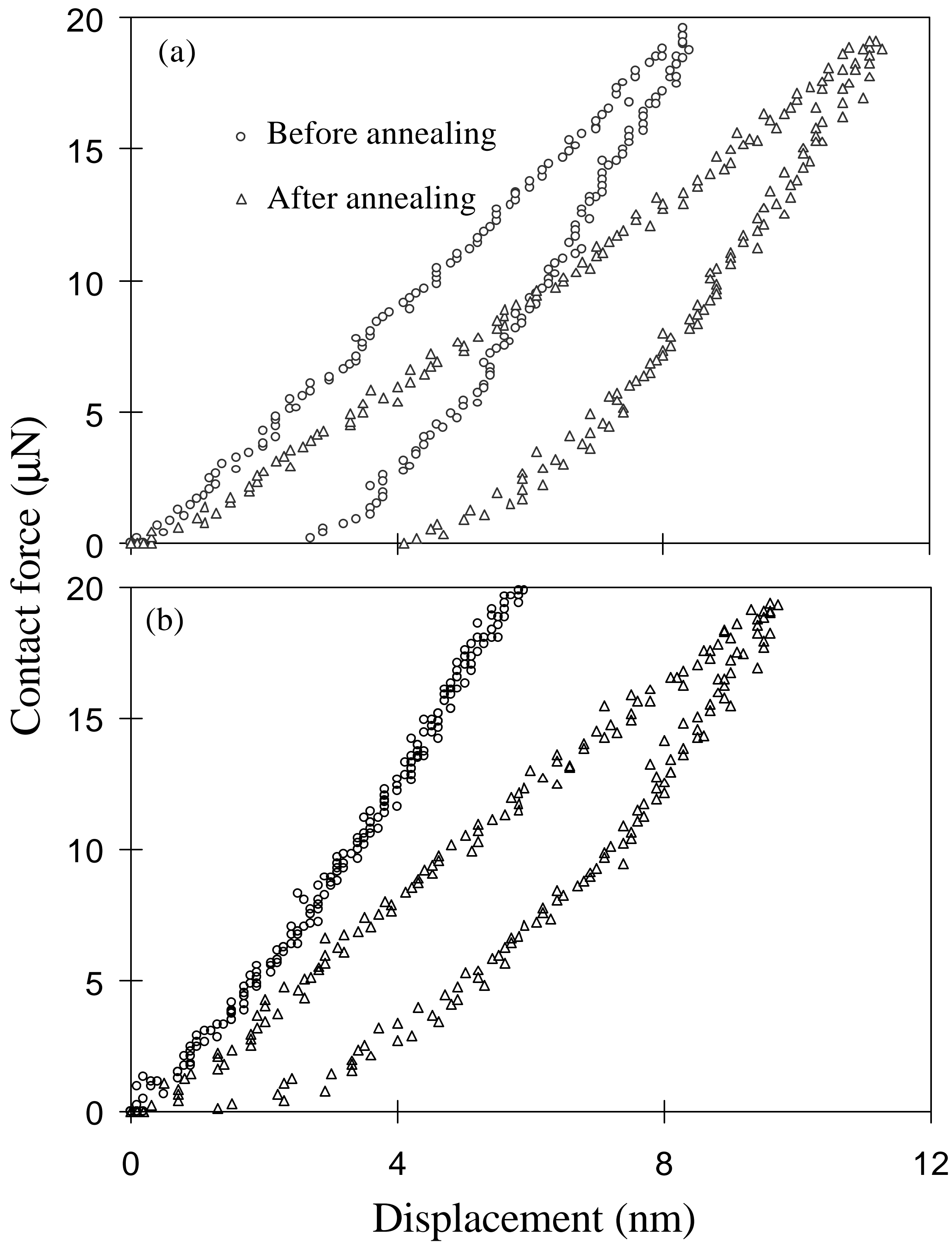

Figure 10

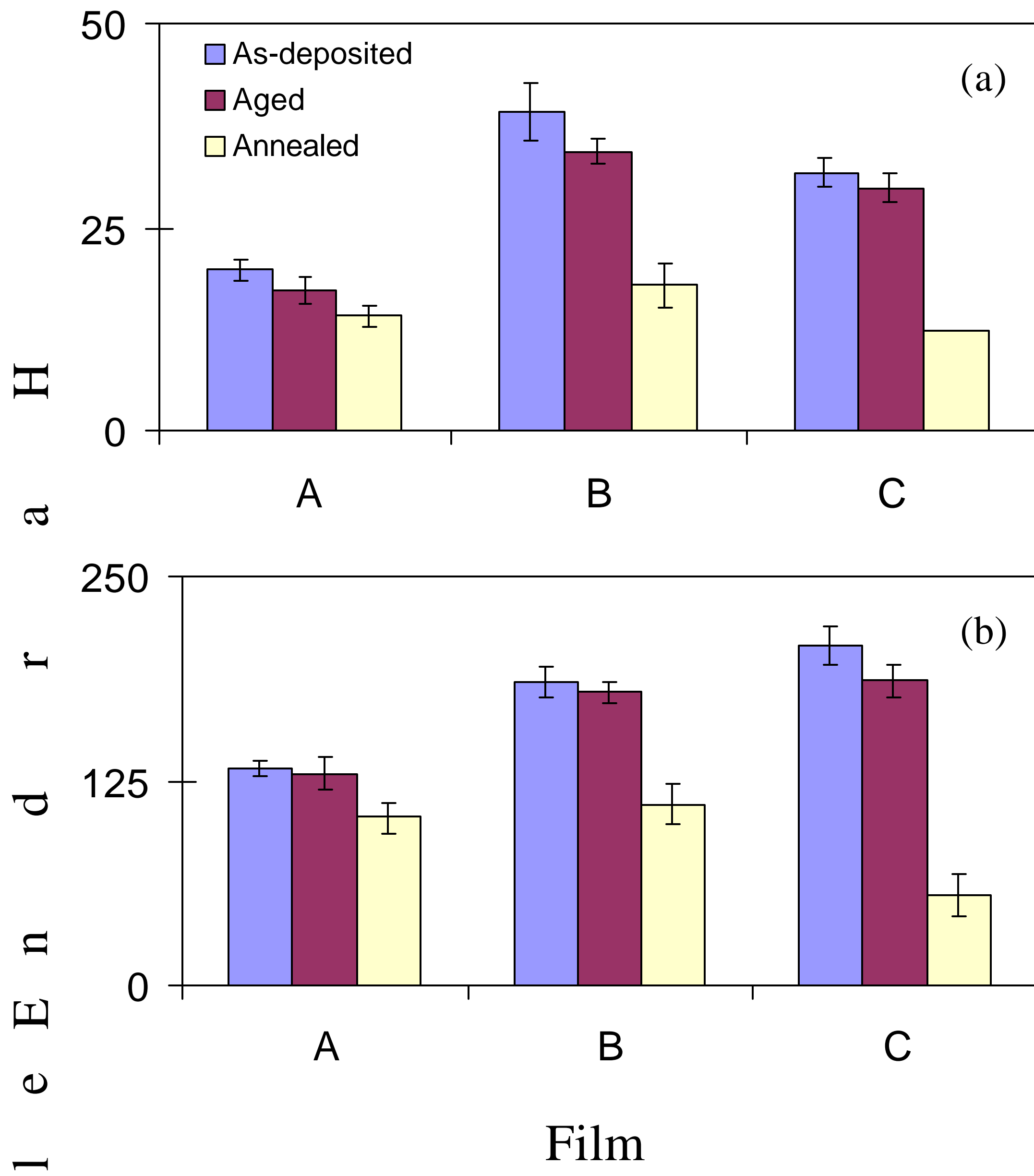

Figure 11

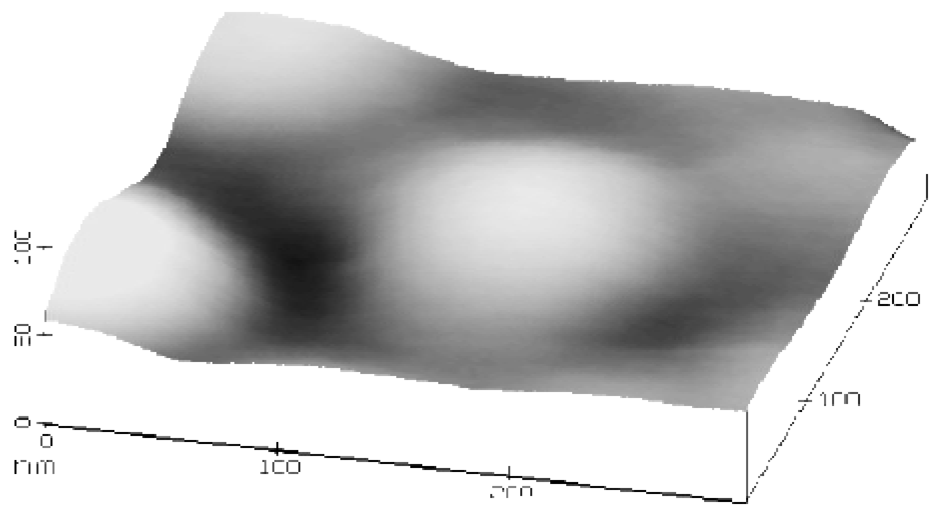

Figure 12

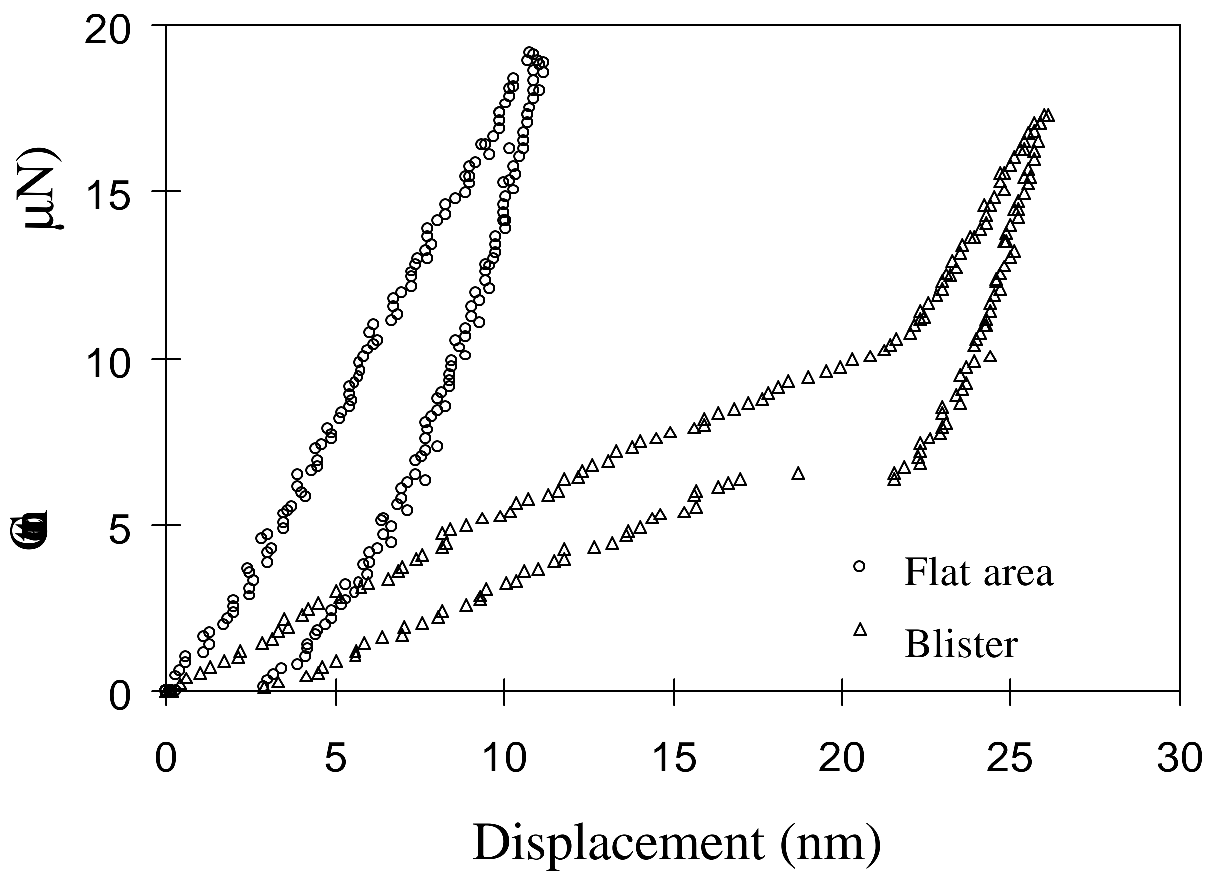

Figure 13

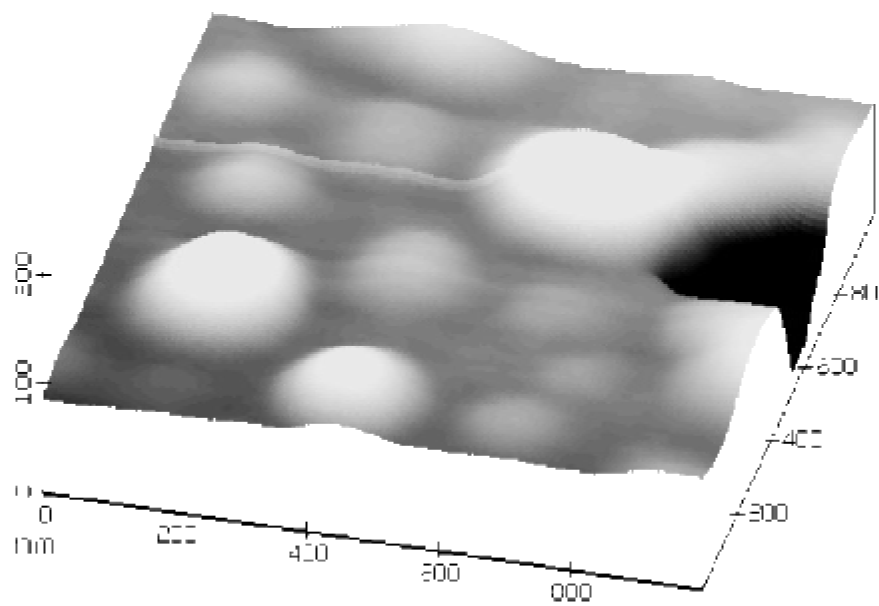

Figure 14